# A Physical Model of Nonstationary Blur in Ultrasound Imaging — Source link

Adrien Besson, Lucien Roquette, Dimitris Perdios, Matthieu Martin Jean-Andre Simeoni ...+4 more authors

Institutions: École Polytechnique Fédérale de Lausanne, IBM, Heriot-Watt University

Topics: Image restoration, Discretization and Context (language use)

Related papers:

- Modeling nonstationary lens blur using eigen blur kernels for restoration

- Maximum Likelihood Parametric Based on a Continuous Spatial Blur Identification Domain Model

- Image Deblurring Based on Physical Processes of Blur Impacts

- Estimation of Motion Parameters for Ultrasound Images Using Motion Blur Invariants

- Blurred image restoration using the type of blur and blur parameter identification on the neural network

Share this paper:  🅕 🆇 in ✉

View more about this paper here: https://typeset.io/papers/a-physical-model-of-nonstationary-blur-in-ultrasound-imaging-49nkp7ppz6

# Fast Non-stationary Deconvolution in Ultrasound Imaging

Adrien Besson, *Student Member, IEEE,* Lucien Roquette, Dimitris Perdios, *Student Member, IEEE,*
Matthieu Simeoni, *Student Member, IEEE,* Marcel Arditi, Paul Hurley, Yves Wiaux,
and Jean-Philippe Thiran, *Senior Member, IEEE,*

*Abstract*—Pulse-echo ultrasound (US) aims at imaging tissue using an array of piezoelectric elements by transmitting short US pulses and receiving backscattered echoes. Conventional US imaging relies on delay-and-sum (DAS) beamforming which retrieves a radio-frequency (RF) image, a blurred estimate of the tissue reflectivity function (TRF). To address the problem of the blur induced by the DAS, deconvolution techniques have been extensively studied as a post-processing tool for improving the resolution. Most approaches assume the blur to be spatially invariant, i.e. stationary, across the imaging domain. However, due to physical effects related to the propagation, the blur is non-stationary across the imaging domain. In this work, we propose a continuous-domain formulation of a model which accounts for the diffraction effects related to the propagation. We define a PSF operator as a sequential application of the forward and adjoint operators associated with this model, under some specific assumptions that we precise. Taking into account this sequential structure, we exploit efficient formulations of the operators in the discrete domain and provide a PSF operator which exhibits linear complexity with respect to the grid size. We use the proposed model in a maximum-a-posteriori estimation algorithm, with a generalized Gaussian distribution prior for the TRF. Through simulations and *in-vivo* experimental data, we demonstrate its superiority against state-of-the-art deconvolution methods based on a stationary PSF.

*Index Terms*—Deconvolution, Point-Spread-Function, Ultrasound Imaging

## I. INTRODUCTION

ULTRASOUND (US) imaging is a widely used medical imaging modality due to its non-invasiveness, relative low-cost and real time capability. By appropriately placing a US probe, usually an array of piezoelectric transducer elements, a medical doctor is able to visualize cross-section images of regions of interest in the body resulting from local variations in density and sound velocity.

The US imaging process exploits the transducer elements for both transmitting acoustic pulses in the region of interest and recording the response of the medium to these pulses as echo signals. The set of these signals is related to the spatial distribution of variations in acoustic impedance, i.e. in medium density and sound velocity, denoted as the tissue reflectivity function (TRF), by a US propagation operator. Due to finite aperture of the probe and bandlimited properties of each transducer element, retrieving the TRF from the echo signals is an ill-posed problem. In standard US imaging, the delay-and-sum (DAS) operator is used as an approximate inverse of the propagation operator. Such an approximation leads to a radio-frequency (RF) image, a blurred estimate of the TRF. The point-spread-function (PSF) is introduced to relate these quantities.

Wave propagation and diffraction in the medium imply that the PSF is spatially varying, as it can be seen in Figure 1. While this is problematic for most deconvolution techniques, accounting for this non-stationarity[1] is the only way to retrieve an accurate estimate of the TRF.

Most of state-of-the-art methods exploit spatially invariant PSF. In several studies, the PSF is estimated in a preliminary step either through *in-vitro* measurements or by simulation [1], [2], [3], [4]. Other approaches estimate directly the PSF on the RF image using homomorphic filtering of the cepstrum [5], [6], [7], inverse filtering based on parametric [8], [9], [10] or non-parametric models [11], [12], [13] and power spectrum equalization [14]. Only few recent studies deal with spatially-varying PSF [15], [16]. But, the proposed methods are either too restrictive in the class of functions the PSF belongs to [15] or too computationally expensive to be used in realistic imaging scenarios [16].

In this work, we address the problem of non-stationary deconvolution in US imaging. More precisely, we propose a continuous spatially-varying PSF operator which accounts for diffraction effects related to US propagation and extends the one presented in our previous work [16]. The proposed model is based on a physical modelling of both the US propagation and the DAS, recently discussed in several studies [17], [18].

A. Besson, D. Perdios, M. Arditi and J.-Ph. Thiran are with the Signal Processing Laboratory 5 (LTS5), Ecole Polytechnique Fédérale de Lausanne, CH-1015, Lausanne, Switzerland.

L. Roquette, M. Simeoni and P. Hurley are with the Cognitive Computing Department, IBM Research, 8803, Ruschlikon, Switzerland.

M. Simeoni is also with Laboratoire de Communications Audiovisuelles (LCAV), Ecole Polytechnique Fédérale de Lausanne, CH-1015, Lausanne, Switzerland.

Y. Wiaux is with the Institute of Sensors, Signals and Systems, Heriot-Watt University, EH14 4AS Edinburgh, United-Kingdom.

J.-Ph. Thiran is also with the Department of Radiology, University Hospital Center (CHUV) and University of Lausanne (UNIL), CH-1011, Lausanne, Switzerland.

---

[1]It has to be noted that the terms "stationarity" and "stationary" are used as synonyms for "spatial invariance" and "spatially invariant", respectively.

It only relies on few assumptions, e.g. Born approximation, propagation of an ideal plane or spherical wavefront and assume 2D propagation and 1D transducer geometry. Such assumptions are rather standard in 2D US imaging. It is therefore far more realistic than a model based on a stationary PSF and less restrictive on the PSF than state-of-the-art non-stationary approaches [15]. We also exploit computationally efficient formulations of the discrete operators involved in the above mentioned models, based on parametric formulations described in our previous work [19], [20], and demonstrate both theoretically and experimentally that they scale well in realistic 2D imaging cases.

We use the proposed model in a maximum-a-posteriori (MAP) estimation algorithm, with a generalized Gaussian distribution (GGD) prior for the TRF [4], [21]. We test the method on an extensive number of experiments, namely a numerical phantom of point reflectors, a numerical calibration phantom and two *in-vivo* carotids, for both diverging wave (DW) and plane wave (PW) imaging. We demonstrate that it leads to an improvement of the lateral and axial resolutions on both the point-reflector and the calibration phantoms and provides a higher visual quality on *in-vivo* carotid images.

The remainder of the paper is organized as follows. Section II introduces the non-stationary PSF operator and Section III describes the corresponding fast formulations. Experimental settings are described in Section IV and results are reported and discussed in Section V. Concluding remarks are given in Section VI.
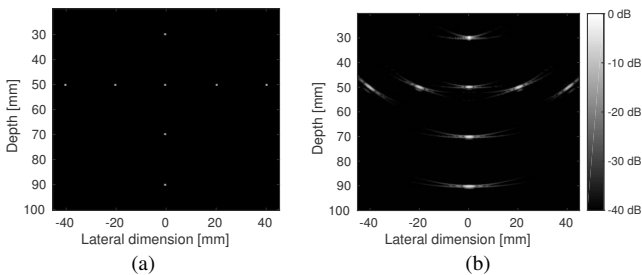


Fig. 1. An example of a TRF (a) and the corresponding demodulated RF image (b) obtained with the DAS operator. We clearly see the spatially varying blur induced by classical beamforming.

## II. MATHEMATICAL MODELLING OF ULTRASOUND IMAGING AND CONTINUOUS LEVEL OPERATORS

In this section, we describe a mathematical formalism of US imaging and propose formulations of the associated operators at the continuous level. Such a formalism is used to introduce a PSF operator that we sequentially split into propagation and DAS operators, which can benefit from fast formulations [19] detailed in Section III.

### A. Mathematical Modelling of Ultrasound Imaging

In a standard US imaging configuration, described in Figure 2, an array of transducer elements is used to propagate an acoustic wave in a medium $\Omega \subset \mathbb{R}^2$ which contains inhomogeneities as local fluctuations in acoustic impedance,
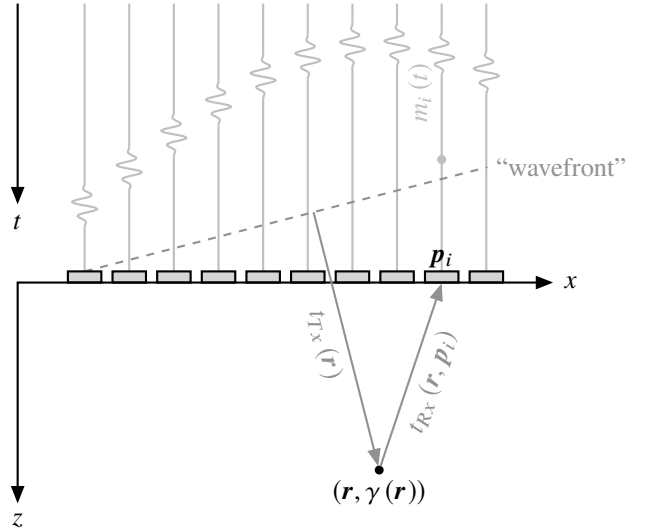


Fig. 2. Standard 2D US imaging configuration (adapted from [19]).

defining the TRF $\gamma \in L_2(\Omega)$ [22], [23], [19]. As a reminder, $L_2(\Omega)$ is the Hilbert space of the square integrable functions which take values in $\Omega$. In addition, for $f, g \in L_2(\Omega)$ we denote their inner product as $\langle f, g \rangle_{L_2(\Omega)}$. Depending on the desired transmit wavefront, e.g. plane wave (PW), diverging wave (DW), focused-wave or synthetic-aperture approaches, each transducer element starts to transmit after a given delay defined by an inter-element delay profile.

In a receive phase, a set of transducer elements, located at $(\boldsymbol{p}_i)_{i=1}^{N_{el}}$, $\boldsymbol{p}_i \in \mathbb{R}^2$, detect echo signals $m_i(t)$, $t \in [0, T]$, defining the following measurements

$$m(t) := \left[ m_1(t), \ldots, m_{N_{el}}(t) \right] \in L_2([0, T])^{N_{el}}, \quad (1)$$

where $L_2([0, T])^{N_{el}} := L_2([0, T]) \times \cdots \times L_2([0, T])$.

The measurements $m(t)$ are related to the TRF $\gamma$ by the propagation of the US wave during the time interval $[0, T]$. It can be demonstrated using the Born approximation that a linear operator $\mathcal{H} : \gamma \mapsto m$, called the propagation operator, relates the TRF to the measurements [17], [19], [20].

Standard US image reconstruction process reconstructs the RF image $\hat{\gamma}$, an estimate of the TRF $\gamma$, which should be ideally close to $\gamma$. This process involves a second operator $\mathcal{D} : m \mapsto \hat{\gamma}$ known as the DAS operator and described in Section II-C.

Using the operators introduced above, we define the US imaging procedure as a mapping between the TRF and the RF image

$$\mathcal{K} : L_2(\Omega) \to L_2(\Omega)$$
$$\gamma \mapsto \hat{\gamma} = \mathcal{D}\mathcal{H}\{\gamma\}. \quad (2)$$

The operator $\mathcal{K}$ is denoted as the PSF operator since it characterizes the blur introduced by the imaging process when approximating $\gamma$ by $\hat{\gamma}$. A further description of the PSF is given in Section II-D.

### B. Ultrasound Propagation Operator

The proposed physical modelling of wave propagation is based on the pulse-echo spatio-temporal impulse response

model introduced by Stepanishen [24]. Furthermore, the effect of the transducer element surface is approximated by a directivity function using a far-field assumption [25]. Under this approximation, we can express the element-raw data received on the $i$-th channel as

$$m_i(t) = \int_{r \in \Omega} o(\boldsymbol{p}_i, \boldsymbol{r}) v_{pe}(t - \tau(\boldsymbol{r}, \boldsymbol{p}_i)) \gamma(\boldsymbol{r}) d\boldsymbol{r}, \qquad (3)$$

where $o(\boldsymbol{p}_i, \boldsymbol{r})$ accounts for the spatial directivity and decay of the reflected wave and $v_{pe}(t)$ is the pulse-echo waveform [26] which depends on the transducer impulse response and the excitation signal. The round trip time-of-flight $\tau(\boldsymbol{r}, \boldsymbol{p}_i)$ is defined as

$$\tau(\boldsymbol{r}, \boldsymbol{p}_i) = t_{Tx}(\boldsymbol{r}) + t_{Rx}(\boldsymbol{r}, \boldsymbol{p}_i), \qquad (4)$$

where $t_{Rx}(\boldsymbol{r}, \boldsymbol{p}_i) = \|\boldsymbol{r} - \boldsymbol{p}_i\|_2 / c$ denotes the propagation delay in receive and $t_{Tx}(\boldsymbol{r})$ is the propagation delay in transmit, supposed to be independent from the location of the emitters assuming a planar wavefront in PW imaging [27] or a spherical wavefront in DW imaging and synthetic aperture approaches [28].

Equation (3) can be compactly expressed in terms of a linear integral operator acting on the TRF $\gamma \in L_2(\Omega)$ and outputting the measurements

$$m(t) = \mathcal{H}\{\gamma\}(t), \qquad (5)$$

where $\mathcal{H} : L_2(\Omega) \to L_2([0, T])^{N_{el}}$ whose $i$-th component is given by

$$(\mathcal{H}\{\gamma\})_i(t) = \int_{r \in \Omega} o(\boldsymbol{p}_i, \boldsymbol{r}) v_{pe}(t - \tau(\boldsymbol{r}, \boldsymbol{p}_i)) \gamma(\boldsymbol{r}) d\boldsymbol{r}. \qquad (6)$$

### C. Delay-and-sum Operator

Starting from the measurements $m(t)$, standard US image reconstruction exploits the well-known delay-and-sum (DAS) algorithm for computing the following RF image:

$$\hat{\gamma}(\boldsymbol{r}) = \sum_{i=1}^{N_{el}} a(\boldsymbol{p}_i, \boldsymbol{r}) m_i(\tau(\boldsymbol{r}, \boldsymbol{p}_i)) \qquad (7)$$

where $a(\boldsymbol{p}_i, \boldsymbol{r})$ accounts for the aperture-apodization weights, commonly applied to reduce the sidelobe levels. The intuition behind DAS is rather simple. In order to estimate the TRF at location $\boldsymbol{r}$, we sum echo signals originating from this point and reaching the transducer elements at each given time-of-flight. Reformulating DAS in terms of a linear integral operator acting on $m(t) \in L_2([0, T])^{N_{el}}$ is also straightforward,

$$\hat{\gamma}(\boldsymbol{r}) = \int_0^T \sum_{i=1}^{N_{el}} a(\boldsymbol{p}_i, \boldsymbol{r}) \delta(t - \tau(\boldsymbol{r}, \boldsymbol{p}_i)) m_i(t) dt$$
$$= \mathcal{D}\{m\}(\boldsymbol{r}), \qquad (8)$$

where $\mathcal{D} : L_2([0, T])^{N_{el}} \to L_2(\Omega)$.

### D. From the Point-Spread-Function Operator to the Point-Spread-Function

We are now equipped with the two operators $\mathcal{D}$ and $\mathcal{H}$ that can be injected in (2) to compute the PSF operator. By following similar arguments to the ones developed in [16], $\mathcal{K}$ can be decomposed as follows,

$$\mathcal{K} : L_2(\Omega) \to L_2(\Omega)$$
$$\gamma \mapsto \int_{s \in \Omega} \gamma(\boldsymbol{s}) k(\cdot, \boldsymbol{s}) d\boldsymbol{s}, \qquad (9)$$

where $k : \Omega \times \Omega \to \Omega$, the bivariate kernel of $\mathcal{K}$, defines the PSF. Moreover, by simple calculations involving $\mathcal{D}$ and $\mathcal{H}$ (derived in [16]), the kernel can be expressed as follows

$$k(\boldsymbol{r}, \boldsymbol{s}) = \sum_{i=1}^{N_{el}} a(\boldsymbol{p}_i, \boldsymbol{r}) o(\boldsymbol{p}_i, \boldsymbol{s}) v_{pe}(\tau(\boldsymbol{r}, \boldsymbol{p}_i) - \tau(\boldsymbol{s}, \boldsymbol{p}_i)). \quad (10)$$

Let us proceed with several comments on the above defined kernel:

- If we assume that $\gamma(\boldsymbol{r}) = \delta(\boldsymbol{r} - \boldsymbol{r}_0)$, with $\boldsymbol{r}_0 \in \Omega$, then

$$\hat{\gamma}(\boldsymbol{r}) = k(\boldsymbol{r}, \boldsymbol{r}_0), \qquad (11)$$

  leading to a natural interpretation of $k$ as the PSF, i.e. the response of the US system to a TRF composed of a single point reflector located at $\boldsymbol{r}_0$;
- In a spatially invariant case, the bivariate kernel $k(\boldsymbol{r}, \boldsymbol{s})$ is simplified to a univariate one leading to $k(\boldsymbol{r}, \boldsymbol{s}) = k(\boldsymbol{r} - \boldsymbol{s})$. Under this approximation, Equation (9) becomes the standard bi-dimensional analytical convolution;
- Considering that $\Omega$ is discretized with $N_g$ grid points, the evaluation of (9) requires $O\left(N_g^2 N_{el}\right)$ operations, which is not compatible with 2D US imaging configurations where $N_g$ is of the order of $10^4$ to $10^6$.

Equipped with the above defined PSF operator, the deconvolution problem can be stated as:

$$\text{Recover } \gamma \text{ from } \hat{\gamma} = \mathcal{K}\{\gamma\}. \qquad (12)$$

### E. Adjoint of the Point-Spread Function Operator

In most deconvolution methods, the adjoint operator $\mathcal{K}^\dagger$ is required to solve Problem (12). For instance, deconvolution approaches that require to solve a convex optimization need to compute the gradient of a data fidelity term, usually expressed using the squared $\ell_2$-norm. Such a gradient is defined as $\mathcal{K}^\dagger(\mathcal{K}\gamma - m)$. At the continuous operator level, the adjoint PSF operator can also be decomposed in terms of the adjoint DAS and adjoint propagation operator,

$$\mathcal{K}^\dagger = \mathcal{H}^\dagger \mathcal{D}^\dagger, \ \mathcal{K}^\dagger : L_2(\Omega) \to L_2(\Omega), \qquad (13)$$

with,

$$\mathcal{H}^\dagger : L_2([0, T])^{N_{el}} \to L_2(\Omega), \ \mathcal{D}^\dagger : L_2(\Omega) \to L_2([0, T])^{N_{el}}.$$

In addition, the adjoint operators $\mathcal{D}^\dagger$ and $\mathcal{H}^\dagger$ are directly obtained from their definitions,

$$\langle \gamma, \mathcal{H}^\dagger m \rangle_{L_2(\Omega)} = \langle \mathcal{H}\gamma, m \rangle_{L_2([0,T])^{N_{el}}}, \qquad (14)$$

$$\langle \gamma, \mathcal{D}m \rangle_{L_2(\Omega)} = \langle \mathcal{D}^\dagger \gamma, m \rangle_{L_2([0,T])^{N_{el}}}, \qquad (15)$$

by simply flipping the order of integration over $\Omega$ and $[0,T]$ [19]. These changes are legitimate thanks to the square integrability of the involved functions.

Consequently, the adjoint operator of the propagation model is given by

$$\mathcal{H}^\dagger\{m\}(r) = \sum_{i=1}^{N_{el}} \int_0^T o(p_i,r)\, m_i(t)\, v_{pe}(t-\tau(r,p_i))\, dt, \quad (16)$$

and the adjoint DAS operator by

$$\left(\mathcal{D}^\dagger\{\gamma\}\right)_i(t) = \int_{r\in\Omega} a(p_i,r)\delta(t-\tau(r,p_i))\gamma(r)dr, \ i=1,...,N_{el}. \quad (17)$$

Interestingly, the adjoint PSF operator can be expressed immediately using the PSF kernel defined in (10), by flipping the two arguments, i.e. using a symmetrised kernel $\tilde{k}(r,s) = k(s,r)$.

## III. Fast Formulations of the Discretized Operators and Resulting Complexity

In this section, we express the deconvolution problem over a regular grid. More precisely, the TRF $\boldsymbol{\Gamma} \in \mathbb{R}^{N_x \times N_z}$ is defined on a regular grid $\Omega_\gamma = \{(x_u, z_v) \in \Omega, u = 1, \ldots, N_x, v = 1, \ldots, N_z\}$ and the RF image $\hat{\boldsymbol{\Gamma}} \in \mathbb{R}^{\hat{N}_x \times \hat{N}_z}$ is defined on a second regular grid $\Omega_{\hat{\gamma}} = \{(x_k, z_l) \in \Omega, k = 1, \ldots, \hat{N}_x, l = 1, \ldots, \hat{N}_z\}$. In Section II, we have established a decomposition of the PSF operator, $\mathcal{K} : L_2(\Omega) \to L_2(\Omega)$ and its adjoint, in terms of the propagation operator $\mathcal{H}$ and DAS operator $\mathcal{D}$. This is a key property when deriving a computationally efficient formulation of the PSF operator relating the TRF to the RF image, each expressed over a specific grid,

$$K : \mathbb{R}^{N_x \times N_z} \to \mathbb{R}^{\hat{N}_x \times \hat{N}_z}, \ \hat{\boldsymbol{\Gamma}} = K\boldsymbol{\Gamma}. \quad (18)$$

In particular, we have the discrete equivalent of the decomposition,

$$\mathcal{K} = \mathcal{D}\mathcal{H} \longrightarrow K = DH, \quad (19)$$

where,

$$D : \mathbb{R}^{N_t \times N_{el}} \to \mathbb{R}^{\hat{N}_x \times \hat{N}_z}, \ H : \mathbb{R}^{N_x \times N_z} \to \mathbb{R}^{N_t \times N_{el}}. \quad (20)$$

The above defined operators allow us to define the discrete counterpart of the continuous deconvolution problem as:

$$\text{Recover } \boldsymbol{\Gamma} \text{ from } \hat{\boldsymbol{\Gamma}} = K\boldsymbol{\Gamma}. \quad (21)$$

The remaining of this section defines fast formulations of the discrete operators $D$ and $H$ from their continuous counterpart. For the sake of simplicity, the grids supporting both the RF and TRF images are assumed to be the same. The pseudo raw-data generated when computing $M = H\boldsymbol{\Gamma} \in \mathbb{R}^{N_t \times N_{el}}$ are expressed with a uniform time spacing

$$M_{ki} = m_i(t_k), \ i=1,\ldots,N_{el}, \ k=1,\ldots,N_t, \quad (22)$$

associated to a given sampling frequency $f_s$.

### A. Fast Propagation Operator and its Adjoint

Based on our previous work [19], the $i$-th component of the integral operator defined in (6) can be reformulated as the following convolution,

$$(\mathcal{H}\{\gamma\})_i(t) = v_{pe} *_t \mathcal{G}_i\{\gamma\}(t), \quad (23)$$

where $*_t$ denotes the analytical convolution over the time dimension and $\mathcal{G}_i : L_2(\Omega) \to L_2([0,T])$ is defined by

$$\mathcal{G}_i\{\gamma\}(t) = \int_{r\in\Omega} o(p_i,r)\,\gamma(r)\delta(t-\tau(r,p_i))dr. \quad (24)$$

Equation (24) can be re-written as the following line integral [19],

$$\mathcal{G}_i\{\gamma\}(t) = \int_{r\in S_i(t)} \frac{o(p_i,r)\gamma(r)}{|\nabla_r g_i(t,r)|} d\sigma(r), \quad (25)$$

where the set of points defining the curve $S_i(t)$ is given by

$$S_i(t) = \{r \in \Omega : g_i(t,r) = 0, \ g_i(t,r) := t - \tau(r,p_i)\}. \quad (26)$$

By appropriate reparameterization of $S_i(t)$ described in our previous work [19], [20], Equation (25) can be expressed as

$$\mathcal{G}_i\{\gamma\}(t) = \int_{\alpha\in\mathbb{R}} \frac{o(p_i,r(\alpha,p_i,t))\gamma(r(\alpha,p_i,t))}{|\nabla_r g_i(t,r(\alpha,p_i,t))|}|J_r|d\alpha, \quad (27)$$

where $r(\alpha,p_i,t) = (\alpha, z(\alpha,p_i,t))$ and $|J_r| : \mathbb{R}^2 \to \mathbb{R}$ denotes the Jacobian associated with the change of variable.

The discretization of the integral over $\alpha$ leads to

$$(\mathcal{H}\{\gamma\})_i(t) \approx v_{pe} *_t \left[\sum_{j=1}^{N_x} w_j(p_i,t)\gamma(r(\alpha_j,p_i,t))\right], \quad (28)$$

where $w_j(p_i,t)$ accounts for the spatial directivity, the decay of the reflected wave, the Jacobian, the gradient of $g$ and the weights related to the numerical approximation of the integral.

Consequently, the application of the discretized forward operator $H$ over the TRF image can be formulated as

$$H\boldsymbol{\Gamma} = V_{pe}\left[\sum_{j=1}^{N_x} W_j \circ I_j \boldsymbol{\Gamma}_{\bullet j}\right] \in \mathbb{R}^{N_t \times N_{el}}, \quad (29)$$

where $\circ$ denotes the Hadamard product, $V_{pe} \in \mathbb{R}^{N_t \times N_t}$ is the Toeplitz matrix associated with the discrete convolution with $v_{pe} = [v_{pe}(t_1), \ldots, v_{pe}(t_{N_t})]^\top$, $I_j : \mathbb{R}^{N_z} \to \mathbb{R}^{N_t \times N_{el}}$ performs the interpolation of the points of the parametric curves at locations $\{z(\alpha_j,p_i,t_k)\}_{k,i=1}^{N_t,N_{el}}$ and $W_j \in \mathbb{R}^{N_t \times N_{el}}$ is defined element-wise as $(W_j)_{ki} = w_j(p_i,t_k)$.

The adjoint operator $\mathcal{H}^\dagger$ defined in Equation (16) can be seen as the following convolution,

$$\mathcal{H}^\dagger\{m\}(r) = \sum_{i=1}^{N_{el}} o(p_i,r)\left(u_{pe} *_t m_i\right)(\tau(r,p_i)), \quad (30)$$

where $u_{pe}(t) = v_{pe}(-t)$ is the matched filter of the pulse-echo waveform.

The adjoint propagation operator $H^\dagger$ expressed over the grid is thus given by,

$$H^\dagger M = \sum_{i=1}^{N_{el}} O_i \circ I_i \left( V_{pe}^\top M_{\bullet i} \right) \in \mathbb{R}^{N_x \times N_z}, \qquad (31)$$

where $O_i \in \mathbb{R}^{N_x \times N_z}$ is defined element-wise as $(O_i)_{kl} = o(p_i, (x_k, z_l))$. The operator $I_i : \mathbb{R}^{N_t} \to \mathbb{R}^{N_x \times N_z}$ performs the interpolation of the time sequence at delay instants $\{\tau((x_u, z_v), p_i)\}_{u,v=1}^{N_x, N_z}$, for $i = 1, \dots, N_{el}$.

### B. Fast Delay-and-sum Operator and its Adjoint

The DAS operator, defined in (7), can be seen as an approximation of the adjoint operator $\mathcal{H}^\dagger$ under the following assumptions:

- The pulse-echo wavelet is a Dirac delta, i.e. $v_{pe}(t) = \delta(t)$;
- The apodization weights replace the spatial directivity and the decay $1/r$ of the reflected wave.

Thus, the application of the discretized DAS operator on the grid is directly defined by the interpolation operation introduced in (31) as

$$DM = \sum_{i=1}^{N_{el}} A_i \circ I_i M_{\bullet i} \in \mathbb{R}^{N_x \times N_z}, \qquad (32)$$

where $A_i \in \mathbb{R}^{N_x \times N_z}$ is defined element-wise as $(A_i)_{kl} = a(p_i, (x_k, z_l))$.

Similarly, the application of the discretized adjoint DAS operator $D^\dagger$ expressed over the grid can be deduced from (29) as

$$D^\dagger \Gamma = \sum_{j=1}^{N_x} W_j \circ I_j \Gamma_{\bullet j} \in \mathbb{R}^{N_t \times N_{el}}, \qquad (33)$$

where the apodization weights $a(p_i, r)$ are used in the computation of $W_j$.

### C. Computation Complexity of the Point-Spread-Function Operator

The application of the discretized PSF operator over the grid $K : \mathbb{R}^{N_x \times N_z} \to \mathbb{R}^{N_x \times N_z}$ requires a priori $O((N_x N_z)^2 N_{el})$ operations using (10). Such a complexity prevents its use in realistic imaging cases, where $N_x N_z$ ranges between $10^4$ and $10^6$ and $N_{el}$ is few hundreds.

To solve the above limitation, we propose to decompose the computation of $K\Gamma$ as follows:

$$K\Gamma = D(H\Gamma), \qquad (34)$$

where $H\Gamma$ is first performed, generating a pseudo raw-data $M$, followed by the application of the DAS $DM$.

The computation of $HX$ requires to perform the following operations:

1) $N_x$ interpolations $I_j \Gamma_{\bullet j}$ where each interpolation has a computational complexity of $O(L N_t N_{el})$ with $L$ the support of the interpolation kernel ($L \ll N_z$);
2) $N_x$ point-wise multiplications with $W_j$, each of which having a cost of $O(N_{el} N_t)$;

3) $N_x$ convolutions with $v_{pe}$ each of which with a complexity of $O(N_t \log N_t)$.

The overall computation complexity of $H\Gamma$ is therefore:

$$\text{Cost}(H\Gamma) = O(L N_x N_{el} N_t + N_x N_{el} N_t + N_x N_t \log N_t) \quad (35)$$
$$= O(N_x N_{el} N_t), \qquad (36)$$

since $\log N_t \ll N_x$ in US imaging.

The computation of $DM$ necessitates rather similar operations as the one described above, apart from the convolution:

1) $N_{el}$ interpolations $I_i M_{\bullet i}$ where each interpolation has a computational complexity of $O(L' N_x N_z)$ with $L'$ the support of the interpolation kernel ($L' \ll N_t$);
2) $N_{el}$ point-wise multiplications with $A_i$, each of which having a cost of $O(N_x N_z)$.

The computational complexity of $DM$ is:

$$\text{Cost}(DM) = O(L' N_{el} N_x N_z + N_{el} N_x N_z) \qquad (37)$$
$$= O(N_{el} N_x N_z). \qquad (38)$$

The overall complexity of the operation $K\Gamma$ can be easily deduced from (36) and (38) as:

$$\text{Cost}(K\Gamma) = O(N_{el} N_x (N_t + N_z)) \qquad (39)$$
$$\approx O(N_{el} N_x N_z), \qquad (40)$$

since $N_t \approx N_z$ in standard US imaging configurations. Thus we have the following:

$$\text{Cost}(KX) \ll O((N_x N_z)^2 N_{el}). \qquad (41)$$

An equivalent reasoning for the computation of the adjoint operation $K^\dagger \hat{\Gamma}$ leads to the same computational complexity as the forward operation. Indeed, the only difference between the two computations resides in the convolution which is negligible in the computational cost.

Thus, the proposed sequential split assumption results in a significant decrease of the computational complexity from quadratic to linear with respect to $N_x N_z$. This decrease allows the method to be applied easily in 2D and even 3D configurations.

## IV. Experiments

This section describes the imaging configurations, for both DW and PW, used to evaluate the proposed non-stationary PSF estimation against state-of-the-art methods. It also describes the $\ell_p$-based convex optimization method used to solve (21).

### A. Diverging Wave Imaging Configuration

A simulated experiment is performed with a standard phased-array probe (P4-2v) whose characteristics are given in Table I. A single diverging wave (2.5 MHz, 1-cycle sinusoidal wave) is transmitted with a corresponding virtual point source located at $z_n$ equal to $-2.9$ mm and laterally centered. No apodization is used on transmit.

The data are acquired on a numerical point-reflector phantom with eight reflectors with unit amplitude and located at positions described on Figure 3(a). The simulation software used in this experiment is Field II [26].

TABLE I
PROBE CHARACTERISTICS

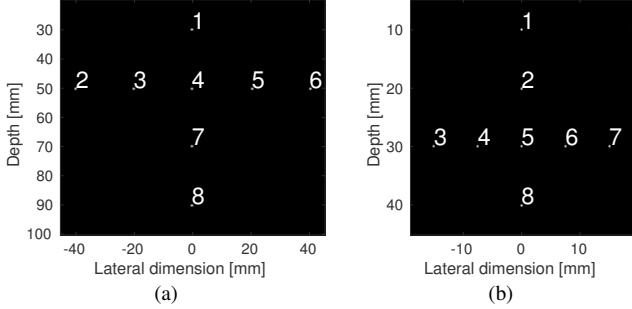| | Diverging wave P4-2v | Plane wave L11-4v | Plane wave L12-5 50mm |
|---|---|---|---|
| Element number | 64 | 128 | 128 |
| Center frequency | 2.7 MHz | 5.133 MHz | 7.8 MHz |
| Sampling frequency | 10.8 MHz | 20.832 MHz | 31.2 MHz |
| Element width | 255 μm | 270 μm | Unknown |
| Element height | 130 μm | 500 μm | Unknown |
| Pitch | 280 μm | 300 μm | 195 μm |
| Elevation focus | 60 mm | 20 mm | Unknown |



Fig. 3. Numerical point-reflector phantoms used for (a) diverging wave and (b) plane wave imaging configurations.

### B. Plane Wave Imaging Configurations

Two standard linear-array probes, namely the L11-4v and the L12-5 50mm, whose characteristics are given in Table I are used.

The L11-4v is used in two simulated configurations (using Field II) for which a single plane wave (5 MHz, 2.5-cycles, square wave) with normal incidence is transmitted without apodization:

- A point-reflector phantom with reflectors described in Figure 3(b);
- The PICMUS numerical phantom[2], whose example B-mode image is displayed on Figure 4.

The L12-5 50mm is used to acquire *in vivo* measurements of two carotids on a Verasonics US scanner (Redmond, WA, USA). A single plane wave (5 MHz, 1-cycle, tri-state waveforms) with normal incidence is transmitted without apodization.
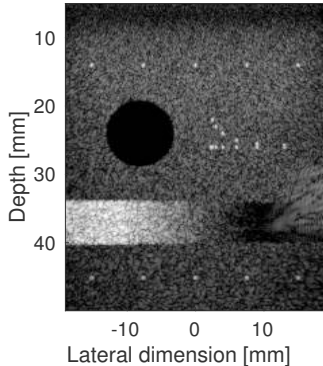


Fig. 4. Log-compressed B-mode image of the PICMUS numerical phantom.

[2]https://www.creatis.insa-lyon.fr/EvaluationPlatform/picmus/index.html

### C. Proposed $\ell_p$-based Deconvolution Method

We use a $\ell_p$-norm minimization, one of the most recent methods introduced in US image deconvolution [4], [29], [21], [30], [12], [16]. Since the discretized PSF operator has been described as a tensor in Section III-A, we have to introduce the reshaping operator $\boldsymbol{P} : \mathbb{R}^{N_x \times N_z} \to \mathbb{R}^{N_x N_z}$, such that $\boldsymbol{\gamma} = \boldsymbol{P}\boldsymbol{\Gamma} \in \mathbb{R}^{N_x N_z}$. We are therefore interested in solving the following optimization problem,

$$\min_{\tilde{\boldsymbol{\gamma}} \in \mathbb{R}^{N_x N_z}} \lambda \left\| \tilde{\boldsymbol{\gamma}} \right\|_p^p + \frac{1}{2} \left\| \hat{\boldsymbol{\gamma}} - \tilde{\boldsymbol{K}} \tilde{\boldsymbol{\gamma}} \right\|_2^2, \qquad (42)$$

where $\tilde{\boldsymbol{K}} = \boldsymbol{P}\boldsymbol{K}\boldsymbol{P}^{\dagger} \in \mathbb{R}^{N_x N_z \times N_x N_z}$ accounts for the discretized PSF operator and $\hat{\boldsymbol{\gamma}} = \boldsymbol{P}\hat{\boldsymbol{\Gamma}} \in \mathbb{R}^{N_x N_z}$, where $\hat{\boldsymbol{\Gamma}}$ is the RF image acquired by the US imaging system. In the objective function minimized in (42), the first term is the prior, the second term is the data-fidelity, $\lambda \in \mathbb{R}_+$ is a regularization parameter and $p$ is a real so that $p \in [1, 2]$ [31]. As a reminder, $\|\boldsymbol{a}\|_p^p = \sum_{i=1}^{N_s} |a_i|^p$.

The values of $p$ are set to 1, 4/3 or 3/2, depending on the experiment, similar to the values used in [4] since their corresponding proximity operator are analytically defined (Appendix A). The optimization algorithm used to solve the deconvolution problem is the fast iterative shrinkage thresholding algorithm (FISTA) described in Appendix A [32]. FISTA is stopped when the relative error between two consecutive estimates is lower than $10^{-3}$.

Three different PSF estimation techniques are compared:

- The proposed non-stationary PSF;
- A stationary PSF previously simulated on Field II using a phantom made of a single scatterer located at 25 mm for PW imaging and 45 mm for DW imaging;
- A stationary PSF estimated from the data using the method described in [23].

The deconvolution is performed on RF images, obtained by applying the DAS operator on the element-raw data. The image grid spacing is set to one fourth of the wavelength in the lateral direction and one eighth of the wavelength in the axial direction. The apodization used in receive is the element-directivity according to Selfridge *et al.* [25].

The methods are implemented using MATLAB[3]. For the non-stationary PSF, the reshaped operators $\boldsymbol{P}\boldsymbol{H}$ and $\boldsymbol{D}\boldsymbol{P}^{\dagger}$ are stored as sparse matrices. For the stationary PSF, the forward and adjoint operator are computed in the Fourier domain.

## V. RESULTS AND DISCUSSION

### A. Point-reflector Experiment

For these experiments, the $\ell_p$-deconvolution is tested with a value of $p$ equal to 1 since we are dealing with sparse images. The comparison is based on the axial and lateral resolution, calculated as the full-width-at-half maximum (FWHM) [33] computed on the log-compressed B-mode image. The regularization parameter is empirically set to its highest value so that all the point reflectors are visible, if possible.

In the DW experiment whose configuration is described in Figure 3(a), Figure 5 shows that the proposed method significantly outperforms the techniques based on a stationary

[3]https://github.com/AdriBesson/epfl-ibm-code

PSF, for both the lateral and the axial resolution. Figure 7 shows the B-mode images of the point-reflectors for standard DAS beamforming (top row), deconvolution with the proposed method (middle row) and deconvolution with the estimated PSF (bottom row). It corroborates the above analysis and shows the superiority of the proposed method. Such results were expected due to the non-stationarity of the PSF, noticeable on the first row of Figure 7.
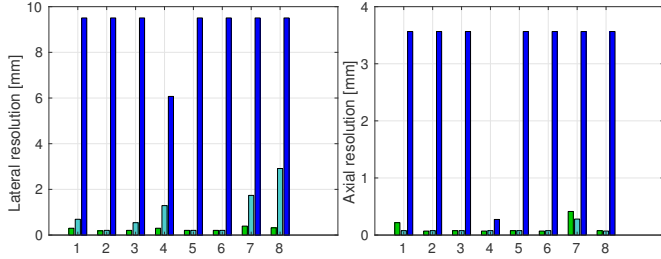


Fig. 5. Lateral and axial resolution of the $\ell_1$-deconvolution of the 8 point reflectors of the DW imaging phantom (Fig. 3(a)) with the proposed non-stationary PSF (green), the estimated stationary PSF (light blue) and the simulated stationary PSF (dark blue).

When using the method with a simulated stationary PSF, it can be noted that the values for both the axial and the lateral resolution are not satisfactory, except for point-reflector 4. This is due to the fact that the PSF used in the deconvolution experiment has been simulated with a point-reflector centered at 45 mm, close to point-reflector 4. The high peaks that one may observe on Figure 5 are due to the fact that several points are not reconstructed. Regarding the method with an estimated PSF, the results are better. This can be explained by the fact that the estimated PSF returns a sort of "averaged PSF" over the entire image, resulting in a rather uniform value of the resolution. We can nevertheless observe a non-uniformity of the resolution with respect to depth (point-reflectors 7 and 8), which emphases the inability of the method to capture non-stationary blur.

In the PW experiment, it can be noticed on Figure 6 that the proposed approach is either close to or better than the best of the methods based on a stationary PSF, which means that it represents a best compromise between lateral and axial resolution. However, the results are less striking than for the DW experiment which is justified by the reduced non-stationarity of the blur compared to the DW experiment.
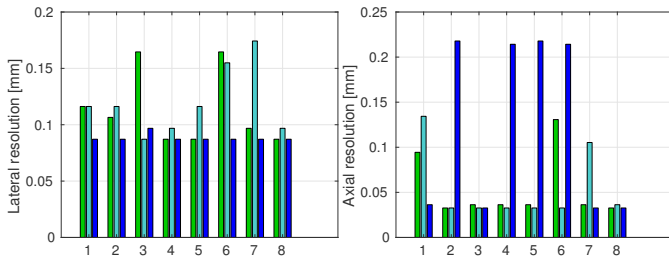


Fig. 6. Lateral and axial resolution of the 8 point reflectors of the PW imaging phantom (Fig. 3(b)) for the $\ell_1$-deconvolution with the proposed non-stationary PSF (green), the estimated stationary PSF (light blue) and the simulated stationary PSF (dark blue).

Regarding the simulated PSF, while the lateral resolution

is relatively constant along the image, the values of the axial resolution is varying significantly. This is due to our choice of regularization parameter. Indeed, it is set so that all the point-reflectors are visible. When the regularization parameter is too high, the first point-reflectors that vanish are point-reflectors 3 and 7 since they are the ones with the highest mismatch with the centered PSF pattern used in the deconvolution.

With a close look on Figs. 5 and 6 , one may highlight some non-uniformity in the values of the resolution obtained with the proposed method. This can be explained by several approximations made in the model:

- no three-dimensional propagation: The proposed model neglects the effects related to the three-dimensional propagation in the Field II simulation, especially the element height and the elevation focus;
- planar/spherical wavefront assumption: We assume that a planar or spherical wavefront, for PW and DW respectively, of constant amplitude propagates in the medium;
- grid mismatch induced by the discretization of the continuous propagation operator and the continuous medium.

### B. PICMUS Phantom Experiment

In this experiment, we compare the methods based on the dB-contrast-to-noise ratio (CNR) and lateral and axial resolution, computed on the PICMUS phantom displayed in Figure 4. The CNR [33] is a measure of the contrast, calculated on the normalized envelope image, i.e. on the envelope image divided by its maximum value, as follows,

$$\text{CNR} = 20 \log_{10} \frac{|\mu_t - \mu_b|}{\sqrt{\frac{\sigma_t^2 + \sigma_b^2}{2}}}, \quad (43)$$

where $(\mu_t, \mu_b)$ and $(\sigma_t^2, \sigma_b^2)$ are the means and the variances of the target inclusion (anechoic region of Figure 4) and the background, respectively.

The results are reported in Table II for the $\ell_p$-deconvolution, with $p = 1.3$ and $1.5$, and with the proposed non-stationary PSF as well as the two stationary ones. We choose to show the results for one specific value of the regularization parameter which recovers acceptable images based on visual assessment, but the results remain stable in a wide range of values[4].

On Table II, one can see that the proposed PSF outperforms the other methods, for nearly all the cases. For the axial resolution at 45 mm, it appears that the method with the simulated PSF is slightly better than the proposed method. It may be due to some assumptions made in the proposed model of the PSF, described in Section V-A. It can be noticed that the improvement of the proposed method in terms of resolution is slight, which is in accordance with the results of Section V-A.

Regarding the results of the deconvolution procedure, we observe that $p = 1.3$ leads to better resolution but lower contrast than $p = 1.5$. This can be explained by a close look to the definition of the CNR. Indeed, it may be deduced from (43) that the CNR favors piecewise-continuous regions where $\sigma_b$ and $\sigma_t$ tend to 0. On the contrary, high-resolution images exhibit more "spiky" behaviour in speckle region

---

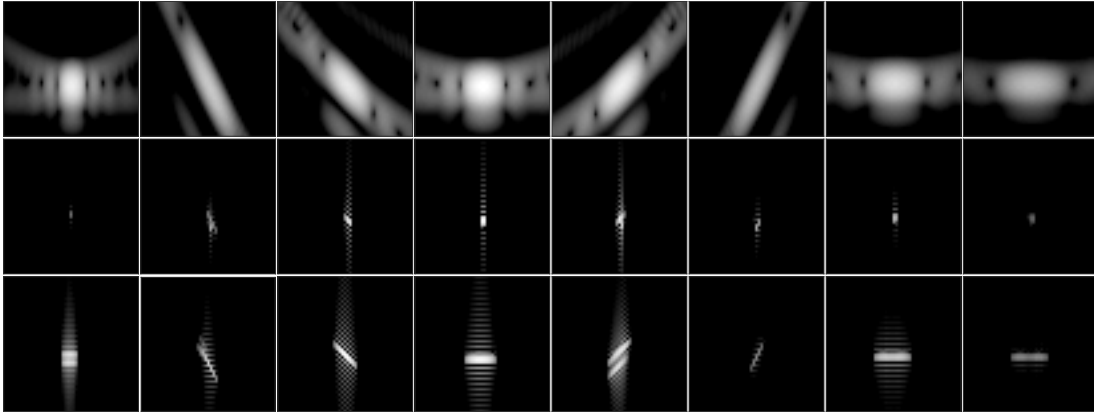[4]https://github.com/LTS5/us-non-stationary-deconv

Fig. 7. Log-compressed (40 dB dynamic range) B-mode images of point-reflector 1 to point-reflector 8 (from left to right) of the DW configuration (Fig. 3(a)) obtained with standard DAS beamforming (top row), deconvolution with the proposed method (middle row) and deconvolution with the estimated PSF (bottom row).

than low-resolution images which usually result in lower mean and higher variance, therefore in a lower CNR. In $\ell_p$-deconvolution, the value of $p$ impacts the shape of the GGD prior, resulting in variation of the resolution of the recovered TRF. The lower $p$, the tighter the shape of the prior, the better the resolution and the lower the CNR.

TABLE II
COMPARISON OF THE METHODS ON THE NUMERICAL PICMUS PHANTOM

| Value of $p$ | CNR [dB] | Method | Lat. Res. [mm] | | Ax. Res. [mm] | |
| | | | 14 mm | 45 mm | 14 mm | 45 mm |
|---|---|---|---|---|---|---|
| $p = 1.5$ | 6.60 | Prop. PSF | **0.22** | **0.37** | **0.22** | 0.27 |
| | | Est. PSF | 0.26 | 0.48 | 0.25 | 0.31 |
| | | Sim. PSF | 0.30 | 0.41 | 0.26 | **0.26** |
| $p = 1.3$ | 6.00 | Prop. PSF | **0.16** | **0.29** | **0.15** | 0.25 |
| | | Est. PSF | 0.18 | 0.41 | 0.18 | 0.23 |
| | | Sim. PSF | 0.25 | 0.35 | 0.19 | **0.19** |

### C. In-vivo Carotid Experiments

Due to the lack of ground truth and appropriate quality metric for *in-vivo* images, the comparison between the methods is limited to a visual assessment in this Section.

Low resolution demodulated RF images of the two carotids, obtained by DAS beamforming without deconvolution, are displayed on Figs. 8(a) and 8(e). The B-mode images of the $\ell_p$-deconvolution technique for the first carotid, and for $p = 1.5$, are displayed on Figs. 8(b), 8(c) and 8(d). The B-mode images of the $\ell_p$-deconvolution technique for the second carotid, and for $p = 1.3$, are displayed on Fig. 8(f), 8(g) and 8(h).

It can be noticed that the deconvolution methods all lead to significantly higher resolution than the demodulated RF images. The deconvolution effect is more pronounced for the proposed method and the estimated PSF than for the simulated PSF. This can be seen on the artery wall. In addition, the proposed method allows a better reconstruction of the textured area, such as the speckle region under the lower artery wall, than both methods based on a stationary PSF.

### D. Preliminary Computational Times on a Parallel Platform

The results discussed in the previous sections are based on MATLAB implementations which are obviously not compatible with real-time requirements. To give a flavour of the potential for parallelizability of the proposed approach, we evaluate a preliminary implementation of the operators on a graphical processing unit (GPU). Since the implementation is neither fully validated nor optimized, it has not been used to produce the results presented in this work and will be described in a fully dedicated publication.

The sequential application of $\boldsymbol{D}$ and $\boldsymbol{H}$ takes around 50 ms for the *in-vivo* carotid image case, a NIVIDIA Titan X GPU platform, which is similar to the timings presented in previous publications [19], [20]. For the DW imaging case, the lower number of transducer elements and lower sampling frequency are compensated by the higher number of grid points, due to the wider field of view, resulting in similar computation times. Regarding the adjoint operator $\boldsymbol{D}^\dagger$ and $\boldsymbol{H}^\dagger$, the computation times are also very similar to the ones observed for the forward operators which makes sense since they exhibit similar computational complexity.

The computation times of both operators scale linearly with the number of transducer elements, the number of time samples and the number of grid points which is compatible with the complexity derived in Section III-C.

Again, it has to be noticed that the proposed implementations are not optimal and substantial gain may be achieved by working on simple acceleration strategies. However, it is rather reasonable to argue that the proposed method, while more complex than stationary strategies, scales quite well with large amount of data and may be compatible with real time 2D- as well as 3D-imaging.

## VI. CONCLUSION

This work presents a model of a spatially-varying point spread function (PSF) in the context of 2D ultrasound imaging. A mathematical formulation of the PSF operator is derived as a mapping from the tissue reflectivity function (TRF) to its blurred estimate denoted as the radio-frequency image (RF). The proposed formulation is based on a sequential split of
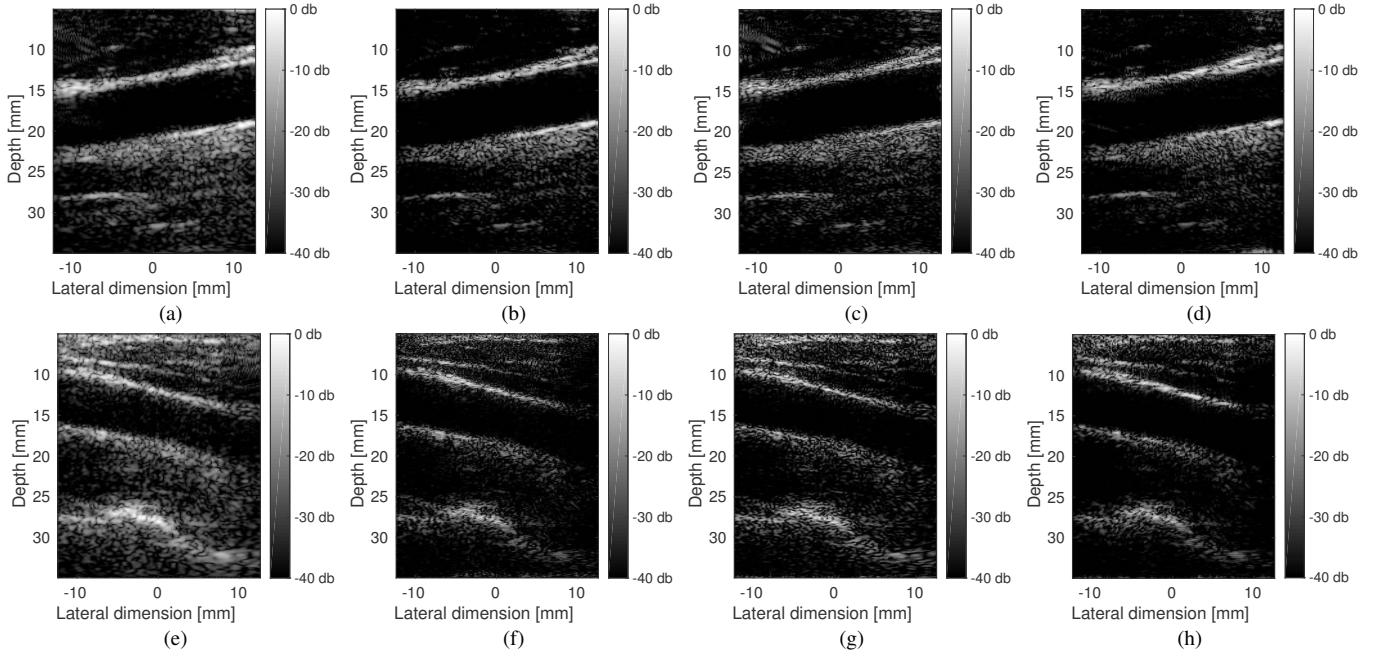
Fig. 8. (a)-Low resolution (LR) image of carotid 1; HR image obtained for $p = 1.5$ with (b)-the proposed method, (c)-the estimated PSF and (d)-the simulated PSF; (e)-LR image of carotid 2; High resolution (HR) image obtained for $p = 1.3$ with (f)-the proposed method, (g)-the estimated PSF and (h)-the simulated PSF.

the PSF into a propagation operator which relates the TRF to the measured echo signals, and a DAS operator which forms the RF image from the echo signals. The two operators are interpreted in terms of the pulse-echo spatio-temporal impulse response model in the continuous domain and benefit from computationally efficient discrete counterparts based on parametric formulations of time-of-flight equations and interpolation on appropriate grids. Such formulations allow the PSF operator to scale linearly with the number of image grid points and make non-stationary deconvolution compatible with real-time applications when implemented on parallel architectures.

The proposed model of the PSF is injected into a maximum-a-posteriori deconvolution algorithm and it is demonstrated through simulated and *in vivo* examples that the deconvolution approach with the proposed kernel outperforms the most recent state-of-the-art deconvolution methods based on a stationary kernel in terms of image quality. We eventually discuss some possible improvements of the proposed model, i.e. by leveraging the planar or spherical wavefront assumption and taking into account effects related to the 3D propagation.

## APPENDIX A
### FAST ITERATIVE SHRINKAGE THRESHOLDING ALGORITHM AND PROXIMITY OPERATORS

#### A. Fast Iterative Shrinkage Thresholding Algorithm

This section briefly presents the fast iterative shrinkage thresholding algorithm (FISTA) used to solve Problem (42). For an in-depth description of the method, please refer to [32]. FISTA is an accelerated version of the well-known iterative soft thresholding algorithm (ISTA), that can be used to solve the following problem:

$$\min_{x \in \mathbb{R}^N} \|y - Ax\|_2^2 + \phi(x),\qquad(44)$$

where $y \in \mathbb{R}^M$, $x \mathbb{R}^N$, $A \in \mathbb{R}^{M \times N}$, $\phi : \mathbb{R}^N \rightarrow \mathbb{R}$ is a non-smooth convex regularizer.

In order to solve Problem (44), FISTA is composed of an acceleration step and a proximal gradient steps described in Algorithm 1. The proximal gradient step involves the following proximity operator [34]:

$$\text{prox}_\phi(x; \lambda) = \arg\min_{z \in \mathbb{R}^N} \lambda\phi(z) + \frac{1}{2}\|z - x\|_2^2.\qquad(45)$$

---

**Algorithm 1** FISTA used to solve Problem (44)

**Require:** $A, \phi, y, L \geq \lambda_{max}(A^T A)$
  **initialization:** $i = 1, t_0 = 1, x_{-1} = x_0 = 0$
  **repeat**
    $t_i \leftarrow \frac{1+\sqrt{1+4t_{i-1}^2}}{2}, \quad \alpha_i \leftarrow \frac{1-t_{i-1}}{t_i}$
    $c_i \leftarrow \alpha_i x_{i-2} + (1 - \alpha_i) x_{i-1}$
    $x_i \leftarrow \text{prox}_\phi\left(c_i + \frac{1}{L}A^T(y - Ac_i); \frac{1}{L}\right)$
    $i \leftarrow i + 1$
  **until** stopping criterion
  **return** $x_i$

---

In Algorithm 1, $\lambda_{max}(A^T A)$ denotes the highest eigenvalue of $A^T A$.

#### B. Proximity operators associated with the $\ell_p$-norm

We consider the proximity operator defined in (45), where $\phi(x) = \|x\|_p^p$ and $p \geq 1$. Thanks to the separability of the two functions involved in the proximity operator, the problem can

be solved element-wise. According to Table 10.2 of [34], the following equivalence holds:

$$z_i = \arg \min_{z_i \in \mathbb{R}} \lambda |z_i|^p + \frac{1}{2} (z_i - x_i)^2, \ \forall (x_i, z_i) \in \mathbb{R} \times \mathbb{R}, \ \lambda > 0 \tag{46}$$

$$\Leftrightarrow z_i = \text{sign}(x_i) q, \ q \geq 0, \ q + p\lambda q^{p-1} = |x_i|. \tag{47}$$

Thus, in order to derive the proximity operator associated with the $\ell_p$-norm, one has to solve (47), which, in the general case, involves finding roots of a polynomial with arbitrarily high degree and can be achieved using Newton's method.

For specific values of $p$, the polynomial may have a degree lower or equal to 3. In such cases, (47) has an analytical solution. This is the case for the values of $p$ considered in the study:

*a) Case $p = 1$:* The solution of (47) is immediately deduced as:

$$z_i = \text{sign}(x_i) \max(|x_i| - \lambda, 0), \tag{48}$$

which is the well-known soft-thresholding operator.

*b) Case $p = 3/2$:* The solution of (47) involves to find the positive root of the following polynomial of order 2:

$$0 = q + \frac{3}{2}\lambda q^{1/2} - |x_i| \tag{49}$$

$$\Leftrightarrow 0 = q^2 - \left(2|x_i| - \frac{9}{4}\lambda^2\right) q + x_i^2, \ |x_i| \geq q \tag{50}$$

$$\Leftrightarrow q = |x_i| + \frac{9}{8}\lambda \left(\lambda - \sqrt{\frac{16}{9}|x_i| + \lambda^2}\right). \tag{51}$$

*c) Case $p = 4/3$:* The solution of (47) involves to find the positive root of the following polynomial of order 3:

$$0 = q + \frac{4}{3}\lambda q^{1/3} - |x_i| \tag{52}$$

$$\Leftrightarrow 0 = q^3 - 3|x_i|q^2 + \left(3|x_i|^2 + \frac{64}{27}\lambda^3\right) q - |x_i|^3. \tag{53}$$

Using Cardano's method and after several calculations not detailed here, one may obtain the following value of $q$:

$$q = |x_i| + \frac{1}{9} \left(\frac{16 \cdot 2^{1/3} \cdot \lambda^2}{(z + 27|x_i|)^{1/3}} - 2\lambda (z + 27|x_i|)^{1/3}\right) \tag{54}$$

$$z = \sqrt{256\lambda^3 + 729|x_i|^2}. \tag{55}$$

## References

[1] W. Vollmann, "Resolution enhancement of ultrasonic B-scan images by deconvolution," *IEEE Trans. Sonics Ultrason.*, vol. 29, no. 2, pp. 78–82, mar 1982.

[2] C. N. Liu, M. Fatemi, and R. C. Waag, "Digital processing for improvement of ultrasonic abdominal images," *IEEE Trans. Med. Imaging*, vol. 2, no. 2, pp. 66–75, jun 1983.

[3] T. Loupas, S. D. Pye, and W. N. McDicken, "Deconvolution in medical ultrasonics: practical considerations," *Phys. Med. Biol.*, vol. 34, no. 11, pp. 1691–1700, nov 1989.

[4] Z. Chen, A. Basarab, and D. Kouame, "Compressive deconvolution in medical ultrasound imaging," *IEEE Trans. Med. Imaging*, vol. 35, no. 3, pp. 728–737, mar 2016.

[5] U. R. Abeyratne, A. P. Petropulu, and J. M. Reid, "Higher order spectra based deconvolution of ultrasound images," *IEEE Trans. Ultrason. Ferroelectr. Freq. Control*, vol. 42, no. 6, pp. 1064–1075, nov 1995.

[6] T. Taxt, "Comparison of cepstrum-based methods for radial blind deconvolution of ultrasound images," *IEEE Trans. Ultrason. Ferroelectr. Freq. Control*, vol. 44, no. 3, pp. 666–674, may 1997.

[7] T. Taxt and J. Strand, "Two-dimensional noise-robust blind deconvolution of ultrasound images," *IEEE Trans. Ultrason. Ferroelectr. Freq. Control*, vol. 48, no. 4, pp. 861–867, jul 2001.

[8] J. Jensen, "Estimation of in vivo pulses in medical ultrasound," *Ultrason. Imaging*, vol. 16, no. 3, pp. 190–203, jul 1994.

[9] T. Taxt, "Radial homomorphic deconvolution of B-mode medical ultrasound images," in *Proc. 12th IAPR Int. Conf. Pattern Recognit.*, aug 1994, pp. 149–152.

[10] G. Demoment, R. Reynaud, and A. Herment, "Range resolution improvement by a fast deconvolution method," *Ultrason. Imaging*, vol. 6, no. 4, pp. 435–451, oct 1984.

[11] J. Jensen and S. Leeman, "Nonparametric estimation of ultrasound pulses," *IEEE Trans. Biomed. Eng.*, vol. 41, no. 10, pp. 929–936, oct 1994.

[12] O. Michailovich and A. Tannenbaum, "Blind deconvolution of medical ultrasound images: A parametric inverse filtering approach," *IEEE Trans. Image Process.*, vol. 16, no. 12, pp. 3005–3019, dec 2007.

[13] R. Demirli and J. Saniie, "Model-based estimation of ultrasonic echoes part I: Analysis and algorithms," *IEEE Trans. Ultrason. Ferroelectr. Freq. Control*, vol. 48, no. 3, pp. 787–802, may 2001.

[14] D. Iraca, L. Landini, and L. Verrazzani, "Power spectrum equalization for ultrasonic image restoration," *IEEE Trans. Ultrason. Ferroelectr. Freq. Control*, vol. 36, no. 2, pp. 216–222, mar 1989.

[15] O. V. Michailovich, "Non-stationary blind deconvolution of medical ultrasound scans," in *Prog. Biomed. Opt. Imaging - Proc. SPIE*, vol. 10139, mar 2017, p. 101391C.

[16] L. Roquette, M. Simeoni, P. Hurley, and A. Besson, "On an analytical, spatially-varying, point-spread-function," in *2017 IEEE Int. Ultrason. Symp.*, sep 2017.

[17] G. David, J.-L. Robert, B. Zhang, and A. F. Laine, "Time domain compressive beam forming of ultrasound signals," *J. Acoust. Soc. Am.*, vol. 137, no. 5, pp. 2773–2784, may 2015.

[18] G. S. Alberti, H. Ammari, F. Romero, and T. Wintz, "Mathematical analysis of ultrafast ultrasound imaging," *SIAM J. Appl. Math.*, vol. 77, no. 1, pp. 1–25, jan 2017.

[19] A. Besson, D. Perdios, F. Martinez, Z. Chen, R. E. Carrillo, M. Arditi, Y. Wiaux, and J.-P. Thiran, "Ultrafast ultrasound imaging as an inverse problem: Matrix-free sparse image reconstruction," *IEEE Trans. Ultrason. Ferroelectr. Freq. Control*, pp. 1–1, 2017.

[20] A. Besson, D. Perdios, F. Martinez, M. Arditi, Y. Wiaux, and J.-P. Thiran, "USSR: An ultrasound sparse regularization framework," in *2017 IEEE Int. Ultrason. Symp.*, sep 2017.

[21] M. Alessandrini, S. Maggio, J. Poree, L. De Marchi, N. Speciale, E. Franceschini, O. Bernard, and O. Basset, "A restoration framework for ultrasonic tissue characterization," *IEEE Trans. Ultrason. Ferroelectr. Freq. Control*, vol. 58, no. 11, pp. 2344–2360, nov 2011.

[22] M. F. Schiffner and G. Schmitz, "Fast pulse-echo ultrasound imaging employing compressive sensing," in *2011 IEEE Int. Ultrason. Symp.*, oct 2011.

[23] O. Michailovich and D. Adam, "A novel approach to the 2-D blind deconvolution problem in medical ultrasound," *IEEE Trans. Med. Imaging*, vol. 24, no. 1, pp. 86–104, jan 2005.

[24] P. R. Stepanishen, "The time-dependent force and radiation impedance on a piston in a rigid infinite planar baffle," *J. Acoust. Soc. Am.*, vol. 49, no. 1A, pp. 76–76, jan 1971.

[25] A. R. Selfridge, G. S. Kino, and B. T. Khuri-Yakub, "A theory for the radiation pattern of a narrow-strip acoustic transducer," *Appl. Phys. Lett.*, vol. 37, no. 1, p. 35, apr 1980.

[26] J. Jensen and N. Svendsen, "Calculation of pressure fields from arbitrarily shaped, apodized, and excited ultrasound transducers," *IEEE Trans. Ultrason. Ferroelectr. Freq. Control*, vol. 39, no. 2, pp. 262–267, mar 1992.

[27] G. Montaldo, M. Tanter, J. Bercoff, N. Benech, and M. Fink, "Coherent plane-wave compounding for very high frame rate ultrasonography and transient elastography," *IEEE Trans. Ultrason. Ferroelectr. Freq. Control*, vol. 56, no. 3, pp. 489–506, mar 2009.

[28] C. Papadacci, M. Pernot, M. Couade, M. Fink, and M. Tanter, "High-contrast ultrafast imaging of the heart," *IEEE Trans. Ultrason. Ferroelectr. Freq. Control*, vol. 61, no. 2, pp. 288–301, feb 2014.

[29] N. Zhao, Q. Wei, A. Basarab, D. Kouame, and J.-Y. Tourneret, "Blind deconvolution of medical ultrasound images using a parametric model for the point spread function," in *2016 IEEE Int. Ultrason. Symp.*, sep 2016.

[30] R. Morin, S. Bidon, A. Basarab, and D. Kouame, "Semi-blind deconvolution for resolution enhancement in ultrasound imaging," in *2013 IEEE Int. Conf. Image Process.*, sep 2013, pp. 1413–1417.

[31] O. Scherzer, H. Grossauer, F. Lenzen, M. Grasmair, and M. Haltmeier, *Variational Methods in Imaging*, ser. Applied Mathematical Sciences. New York, NY: Springer New York, 2009, vol. 167.

[32] A. Beck and M. Teboulle, "A fast iterative shrinkage-thresholding algorithm for linear inverse problems," *SIAM J. Imaging Sci.*, vol. 2, no. 1, pp. 183–202, jan 2009.

[33] M. C. Van Wijk and J. M. Thijssen, "Performance testing of medical ultrasound equipment: Fundamental vs. harmonic mode," *Ultrasonics*, vol. 40, no. 1-8, pp. 585–591, may 2002.

[34] P. L. Combettes and J.-C. Pesquet, "Proximal Splitting Methods in Signal Processing," in *Fixed-Point Algorithms Inverse Probl. Sci. Eng.* Springer New York, 2011, vol. 49, pp. 185–212.